Cosmological Simulations of Normal-Branch Braneworld Gravity

Fabian Schmidt[1, 2, 3]

[1]*Theoretical Astrophysics, California Institute of Technology M/C 350-17, Pasadena, California 91125-0001, USA**
[2]*Department of Astronomy & Astrophysics, The University of Chicago, Chicago, IL 60637-1433*
[3]*Kavli Institute for Cosmological Physics, Chicago, IL 60637-1433*

We introduce a cosmological model based on the normal branch of DGP braneworld gravity with a smooth dark energy component on the brane. The expansion history in this model is identical to ΛCDM, thus evading all geometric constraints on the DGP cross-over scale r_c. This well-defined model can serve as a first approximation to more general braneworld models whose cosmological solutions have not been obtained yet. We study the formation of large scale structure in this model in the linear and non-linear regime using N-body simulations for different values of r_c. The simulations use the code presented in [1] and solve the full non-linear equation for the brane-bending mode in conjunction with the usual gravitational dynamics. The brane-bending mode is attractive rather than repulsive in the DGP normal branch, hence the sign of the modified gravity effects is reversed compared to those presented in [1].

We compare the simulation results with those of ordinary ΛCDM simulations run using the same code and initial conditions. We find that the matter power spectrum in this model shows a characteristic enhancement peaking at $k \sim 0.7\,h/\mathrm{Mpc}$. We also find that the abundance of massive halos is significantly enhanced. Other results presented here include the density profiles of dark matter halos, and signatures of the brane-bending mode self-interactions (Vainshtein mechanism) in the simulations. Independently of the expansion history, these results can be used to place constraints on the DGP model and future generalizations through their effects on the growth of cosmological structure.

Keywords: cosmology: theory; modified gravity; braneworld cosmology; Dark Energy

I. INTRODUCTION

Braneworld scenarios with infinite extra dimensions have received much interest in recent years, as a possible explanation for the observed accelerated expansion of the universe [2, 3], as well as a way to tackle the cosmological constant problem [4, 5]. The simplest such model is the Dvali-Gabadadze-Porrati (DGP) model [6]. In this model, matter lives on a four-dimensional brane embedded in five-dimensional Minkowski space. The gravity action consists of a five-dimensional Einstein-Hilbert term plus an ordinary, four-dimensional term localized on the brane. Gravity thus is five-dimensional on large scales, and reduces to four-dimensional General Relativity on small scales. The transition is given by the *cross-over scale* r_c, which is defined by the ratio of five- and four-dimensional gravitational constants: $r_c = G^{(5)}/2G^{(4)}$.

There are two branches of homogeneous and isotropic solutions in this model, corresponding to the two possible ways of embedding the brane in (asymptotic) five-dimensional Minkowski space. The self-accelerated branch (*sDGP*) has received attention since it leads to a late-time accelerated expansion of the universe without any dark energy or cosmological constant, if r_c is of order the present Hubble horizon c/H_0. However, this branch of the model is plagued by a ghost instability when perturbed around the de Sitter solution [7–9]. In addition, the expansion history predicted by the self-accelerating DGP model [2] does not appear to fit observations (e.g., [10]). The other, so-called normal branch of the theory (*nDGP*), does not have a ghost instability. However, it does not lead to self-acceleration, so that it is necessary to add a cosmological constant (tension) on the brane [11–14], or, more generally a form of stress energy with negative pressure.

Hence, we are interested in generalizing the normal-branch DGP model in a way that allows it to pass expansion history constraints. Much work is ongoing to extend the DGP braneworld scenario [5, 15, 16], and the proposed models are generally expected to exhibit an expansion history close to ΛCDM, while the phenomenology of the modification to GR is expected to be similar to the normal branch DGP model. However, full cosmological solutions have not been obtained yet. Braneworld-inspired *parametrized* generalizations of DGP have been proposed in [17, 18]. On the one hand, this approach might well capture features of a yet-unknown full generalized braneworld model. On the other hand, these parametrizations do not constitute a well-defined theory.

---

* Present address.

Here, we instead opt for considering a well-defined, albeit somewhat contrived model based on DGP, which nevertheless exhibits some of the features of a generalized braneworld model (see Section II D for a discussion). Our model consists of normal-branch DGP gravity, with a general, smooth quintessence-type dark energy component on the brane tuned so that the resulting expansion history is identical to a ΛCDM model. This model which we call *nDGP+DE* thus satisfies all geometric constraints from, e.g. the cosmic microwave background (CMB) and Supernovae, and leaves the cross-over scale r_c as an almost free parameter of the model. Furthermore, the $r_c \to \infty$ limit of the theory is precisely General Relativity with a cosmological constant. Our main aim in this paper is to study the growth of structure in nDGP+DE in the linear and non-linear regime.

The evolution of linear perturbations in DGP has been studied in [19–22]. On scales smaller than the horizon and the cross-over scale, the model can be described as an effective scalar-tensor theory. The massless scalar degree of freedom corresponds to displacements of the brane and is called the *brane-bending mode*. In linear perturbation theory, the effect of the brane-bending mode is simply to rescale the effective gravitational constant for the dynamical potential (the time-time piece of the metric), while the geodesics of photons (i.e. gravitational lensing) are not affected. In the self-accelerating branch of DGP, the brane-bending mode is repulsive, weakening the effective gravitational force, while it is attractive in the normal branch.

As all viable modified gravity models, DGP contains a non-linear mechanism to restore General Relativity in high-density environments. This is achieved by a strong self-coupling of the brane-bending mode, which becomes effective within a characteristic scale, the so-called Vainshtein radius [23–25]. The Vainshtein radius depends on the mass considered as well as its configuration. While the prefactor of the self-coupling is model-dependent, the form of the coupling is generic and is expected to be universal to braneworld models [15, 22]. For typical structures in the Universe, the Vainshtein radius is of cosmological scale. Hence it is necessary to follow the brane-bending mode and its self-interactions when studying the formation of structure in the Universe. In [1], we presented simulations of the self-accelerating DGP model which self-consistently solve for the brane-bending mode (see also [26]). Here, we present simulations of two nDGP+DE models, extending the studies of non-linear structure formation presented in [1] to the normal branch of DGP, where the effects of modified gravity have the opposite sign.

N-body simulations of normal-branch braneworld models have previously been presented in [18]. The key difference to our simulations is that while we solve the full brane-bending mode equation, [18] employed an approximation where the modified forces are parametrized by an effective density-dependent gravitational constant $G_{\rm eff}(\delta\rho)$. Unfortunately, as already pointed out in [18], this approximation does not recover the correct large-distance behavior for the brane-bending mode, so that in principle artefacts of the approximation might appear even on large scales. Furthermore, the approximation will become worse the higher the resolution of the simulation is. We present a quantitative comparison of our simulations with the $G_{\rm eff}(\delta)$ approximation in Appendix A.

In addition to the matter power spectrum and halo mass function, we show results on the density profiles of halos, and signatures of the Vainshtein mechanism in the simulation results. The results presented in this paper together with [1] can serve as a basis for modeling non-linear structure formation in DGP. A model of some of the results presented here and in [1] in the context of spherical collapse and the halo model will be the subject of a forthcoming paper. Such a model can then be used to constrain DGP and more generalized braneworld models using the wealth of large scale structure observations available (see [27] for a first attempt in the case of $f(R)$ gravity).

The paper is structured as follows. In Section II, we describe the nDGP+DE models in detail, including the evolution of linear perturbations and the Vainshtein mechanism. We describe the simulations in Section III, and present the results in Section IV. We conclude in Section V.

II. DGP MODELS

As a gravitational framework for our nDGP+DE cosmology, we choose the normal branch of the DGP model [2]. However, we add a smooth, quintessence-type dark energy on the brane whose equation of state is adjusted precisely to cancel the unwanted effects of the extra dimension on the expansion history, yielding an expansion history identical to ΛCDM. Hence, *independently* of the expansion history, the cross-over scale r_c is a free parameter which is not constrained anymore to be of order H_0^{-1} in this model. The $r_c \to \infty$ limit of this theory is General Relativity with a cosmological constant.

We will consider flat cosmologies throughout, and consider two cosmologies of the nDGP+DE type: one with $r_c = 500 \, \mathrm{Mpc}$ ("nDGP–1"), and one with $r_c = 3000 \, \mathrm{Mpc}$ ("nDGP–2"). We will also compare our results with the cosmological simulations of the self-accelerating DGP model without dark energy ("sDGP") presented in [1].
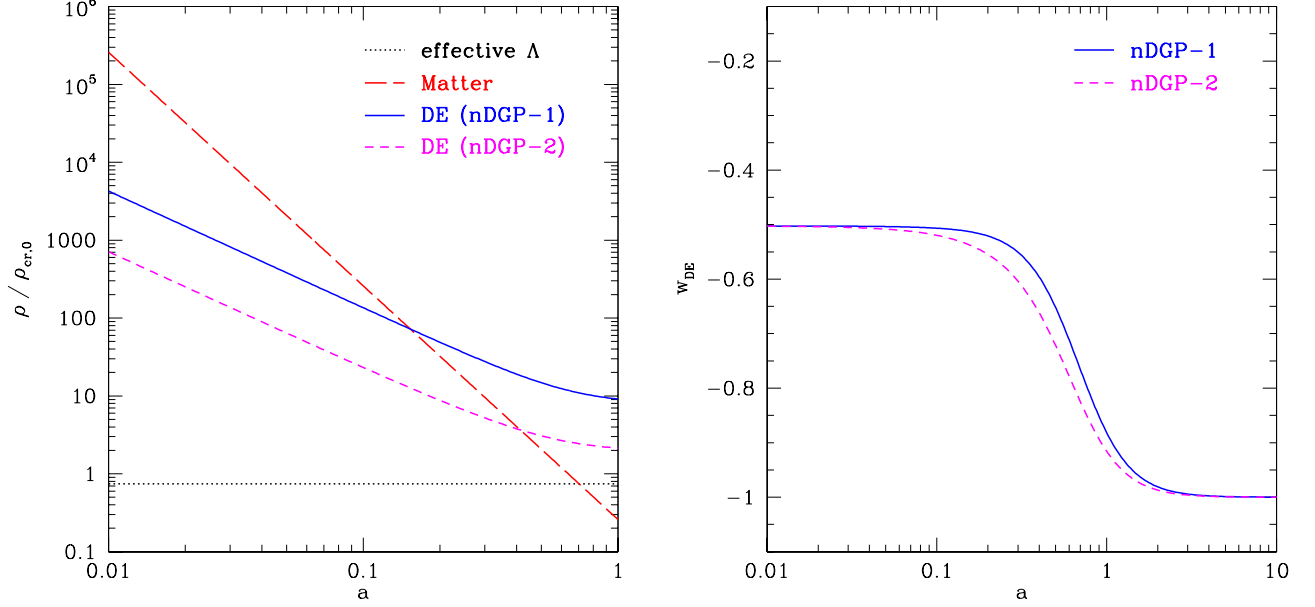
FIG. 1: Behavior of the dark energy component in the nDGP+DE models: density ρ_{DE} and ρ_m, as well as the resulting effective ρ_Λ (*left panel*); equation of state w_{DE} of the dark energy (*right panel*). The model parameters are defined in Tab. I.

A. Background evolution

We start with the modified Friedmann equation for the normal branch of DGP (e.g. [11, 14]):

$$E(a) \equiv \frac{H(a)}{H_0} = \sqrt{\Omega_m a^{-3} + \rho_{\mathrm{DE}}(a)/\rho_{\mathrm{cr},0} + \Omega_{\mathrm{rc}}} - \sqrt{\Omega_{\mathrm{rc}}}, \tag{2.1}$$

where H_0 is the Hubble rate $\dot{a}/a$ today, and

$$\Omega_{\mathrm{rc}} \equiv \frac{1}{4H_0^2 r_c^2}; \quad \Omega_m \equiv \overline{\rho}_{m,0}/\rho_{\mathrm{cr},0}; \quad \rho_{\mathrm{cr},0} = \frac{3H_0^2}{8\pi G}. \tag{2.2}$$

Here $\overline{\rho}_m$ and ρ_{DR} stand for the background energy density of matter and smooth dark energy, respectively. We can now simply equate Eq. (2.1) with the Friedmann equation in GR for a flat ΛCDM universe (with $\Omega_\Lambda = 1 - \Omega_m$):

$$E_{\Lambda\mathrm{CDM}}(a) = \sqrt{\Omega_m a^{-3} + \Omega_\Lambda}. \tag{2.3}$$

and solve for the dark energy density. Note that in this model, one would infer the *correct* value of Ω_m from geometric and early-Universe tests, such as BBN, CMB, SN, and H_0 measurements, which rely on the assumption of the Friedmann equation Eq. (2.3)[1]. This greatly simplifies the interpretation of our results below. We then obtain the following dark energy density: [**Author's note: the following two equations are incorrect in the published version, as pointed out by [28]. I have corrected them here, and show the correct results in Fig. 1. None of the following results, nor those in followup papers, are affected since they simply use the expansion history given in Eq. (2.3).**]

$$\rho_{\mathrm{DE}}(a) = \rho_{\mathrm{cr},0} \left[\Omega_\Lambda + 2\sqrt{\Omega_{\mathrm{rc}}}\sqrt{\Omega_\Lambda + \Omega_m a^{-3}} \right]. \tag{2.4}$$

Note that this energy density is positive definite. In particular, we can derive the following two limits:

$$\rho_{\mathrm{DE}}(a) = \rho_{\mathrm{cr},0} \cdot \begin{cases} 2\sqrt{\Omega_{\mathrm{rc}}\Omega_m}a^{-3/2}, & \Omega_m a^{-3} \gg \Omega_{\mathrm{rc}}, \Omega_\Lambda \\ \Omega_\Lambda + 2\sqrt{\Omega_\Lambda \Omega_{\mathrm{rc}}}, & \Omega_m a^{-3} \ll \Omega_{\mathrm{rc}}, \Omega_\Lambda. \end{cases} \tag{2.5}$$

---

[1] Of course, the interpretation of Λ as a cosmological constant on the other hand would be very misguided.
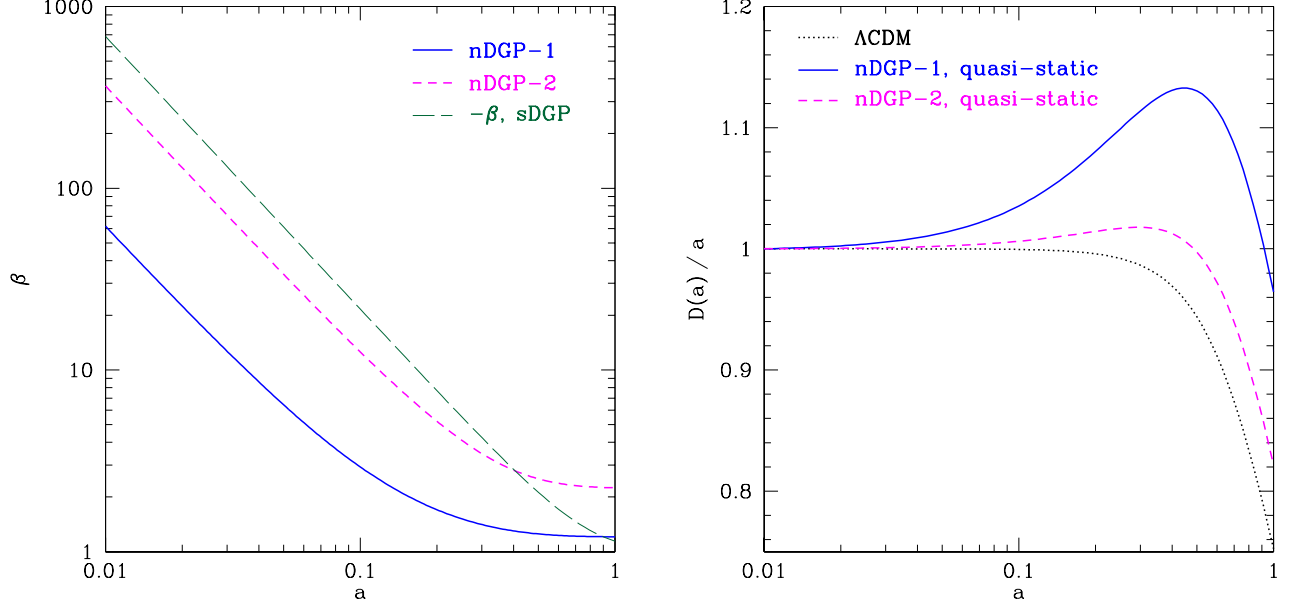
FIG. 2: *Left panel:* The β function Eq. (2.9) in the nDGP+DE models. We also show the function for the self-accelerating DGP model considered in [1] (note that $\beta < 0$ for that model). *Right panel:* Linear growth factor $D(a)/a$ as a function of a, where $D(a)$ is normalized to a in the matter-dominated regime, for ΛCDM and nDGP+DE models in the quasi-static regime ($k \gtrsim 0.01\, h/\mathrm{Mpc}$).

This shows that the equation of state $w_{\mathrm{DE}} = p_{\mathrm{DE}}/\rho_{\mathrm{DE}}$ is always greater than -1: it approaches $-1/2$ for $a \ll 1$, and -1 for $a \gtrsim 1$ (Fig. 1). For $r_c \to \infty$, i.e. $\Omega_{\mathrm{rc}} \to 0$, $\rho_{\mathrm{DE}} = \Omega_\Lambda \rho_{\mathrm{cr},0}$ =const., confirming the ΛCDM limit. Note that in the matter-dominated regime, the dark energy density increases with decreasing cross-over scale r_c (i.e., increasing Ω_{rc}), while at late times, when the DGP term dominates, it becomes independent of r_c and only depends on the effective ΛCDM parameters. Fig. 1 shows the evolution of the dark energy density and the equation of state for the two models we have simulated, nDGP–1 ($r_c = 500\,\mathrm{Mpc}$) and nDGP–2 ($r_c = 3000\,\mathrm{Mpc}$). Ref. [28] provide a quintessential potential which very accurately realizes this time-dependent equation of state.

B. Linear cosmological perturbations

We now consider the evolution of cosmological perturbations in our nDGP+DE model. We work in conformal Newtonian gauge and write the metric as:

$$ds^2 = -[1 + 2\Psi(\mathbf{x}, t)]dt^2 + [1 + 2\Phi(\mathbf{x}, t)]a^2(t)d\mathbf{x}^2 \tag{2.6}$$

Since we assume that the additional dark energy component is smooth, the growth of structure in this model proceeds in the same way as in the normal branch with brane tension [12–14], except that the expansion history is altered. In particular, on small scales $k \gtrsim 0.01\, h/\mathrm{Mpc}$, time derivatives may be neglected with respect to spatial derivatives, which we call the quasi-static regime. If, in addition, $k \gg r_c^{-1}$, DGP reduces to an effective scalar-tensor theory, where the brane-bending mode φ plays the role of the additional degree of freedom. The linearized brane-bending mode equations then lead to a scale-independent but time-dependent modification of the linear growth equation for matter perturbations, $\delta = (\rho - \overline{\rho}_m)/\overline{\rho}_m$ (e.g. [20, 25, 29]):

$$\ddot{\delta} + 2H\dot{\delta} = \frac{k^2}{a^2}\Psi, \quad \left(\frac{k}{aH} \gg 1\right)$$

$$\frac{k^2}{a^2}\Psi = 4\pi G_{\mathrm{lin}}(a)\overline{\rho}_m\delta, \tag{2.7}$$

$$G_{\mathrm{lin}}(a) = G\left(1 + \frac{1}{3\beta(a)}\right), \tag{2.8}$$

where dots denote time derivatives, G is Newton's constant, and, in the normal branch of DGP:

$$\beta(a) = 1 + 2H(a)\, r_c \left(1 + \frac{\dot{H}(a)}{3H^2(a)} \right). \tag{2.9}$$

The function β thus quantifies the departure from GR, which is restored when $\beta \gg 1$ at early times (Fig. 2, left panel). In the normal branch, $\beta > 1$ and hence graviational forces are enhanced by up to $1/3$. Conversely, in the self-accelerating branch $\beta < -1$ and forces are suppressed. Since we only add an additional smooth stress-energy component and do not modify the gravity sector, the changes to standard DGP only come in through the expansion history in Eq. (2.9).

Fig. 2 (right panel) shows the matter growth factor $D(a) = \delta(a)/\delta(a_i)$ in the quasi-static regime as a function of a. The normalization is such that $D(a) = a$ in the matter-dominated regime. As in GR+DE, the growth factor is independent of scale in the quasi-static regime ($k \gg r_c^{-1}$). In this case, the growth is always enhanced in the nDGP+DE models with respect to ΛCDM. On such scales much smaller than r_c, the five-dimensional nature of gravity is not important, and the effect of the attractive brane-bending mode is the cause for the differences to ΛCDM.

More generally, the effect of the brane-bending mode φ on the metric potentials Ψ, Φ on sub-horizon and sub-r_c scales is given by:

$$\Psi = \Psi_N + \frac{1}{2}\varphi, \tag{2.10}$$

$$\Phi = -\Psi_N + \frac{1}{2}\varphi. \tag{2.11}$$

Here, we have defined the "Newtonian" potential Ψ_N via the usual Poisson equation,

$$\frac{k^2}{a^2}\Psi_N = 4\pi G \overline{\rho}_m \delta. \tag{2.12}$$

Note that the propagation of light is not directly affected in DGP, as is usually the case in simple scalar-tensor theories: in the quasi-static regime, the lensing potential $\Phi_- \equiv (\Psi - \Phi)/2$ reduces to Ψ_N. In other words, the relation between Φ_- determining the geodesics of photons and the matter overdensities is unchanged from GR [29].

Finally, on larger scales approaching the horizon, time derivatives as well as the effects of the extra dimension become important. Here, one can use the parametrized post-Friedmann approach [30], calibrated on calculations using the dynamical scaling solution [20], or the full numerical solution [21]. This approach was also used in [14] to place constraints on DGP models with cosmological constant (brane tension), and we adopt the parameters for the normal branch given in [14]. Since we are considering models with r_c smaller than the present horizon scale, care has to be taken on scales significantly larger than r_c where the PPF parametrization has not been calibrated with the full 5D calculation. Such large scales are never relevant for the simulations presented here, however.

Like all N-body simulations, our simulations work in the quasi-static approximation. The full DGP equations contain non-local terms involving $\sqrt{k^2}/r_c$ which could be relevant for small r_c. We verify that neglecting these terms has a negligible impact on the scales probed by the simulations in Section III.

C. Vainshtein mechanism

If the modified force law given by $G_{\rm lin} \neq G$ was valid on all scales, the DGP model would predict order unity deviations from the GR values of post-Newtonian parameters in the Solar System. However, the brane-bending mode φ has self-interactions which suppress its value in high-density regions. In the quasi-static regime, the equation of motion can be written as:

$$\nabla^2\varphi + \frac{r_c^2}{3\beta\, a^2}[(\nabla^2\varphi)^2 - (\nabla_i\nabla_j\varphi)(\nabla^i\nabla^j\varphi)] = \frac{8\pi\, G\, a^2}{3\beta}\delta\rho, \tag{2.13}$$

where $\delta\rho = \overline{\rho}_m\delta$. The motion of particles is then governed by the dynamical potential Ψ as in Eq. (2.10), which receives a contribution from φ. Linearizing Eq. (2.13) together with Eq. (2.10) then yields Eqs. (2.7)–(2.8). For spherically symmetric masses, one can derive an analytic solution to the field equation. Assuming a mass of constant density with radius R (top hat), one obtains the following gravitational acceleration:

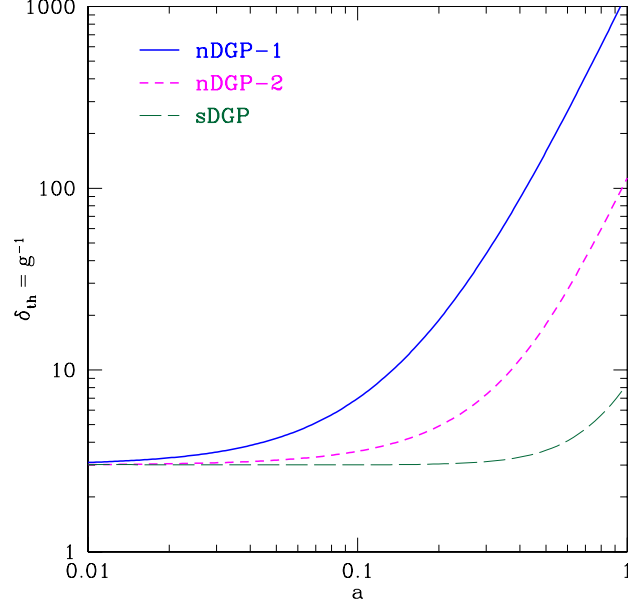$$\mathfrak{g} = \mathfrak{g}_N + \frac{1}{2}\frac{d\varphi}{dr} = \mathfrak{g}_N(r)\,[1 + \Delta(r)], \tag{2.14}$$

FIG. 3: Overdensity threshold for the φ self-interactions, defined as inverse of the non-linearity parameter g [Eq. (2.17)], as a function of scale factor in the different DGP cosmologies.

$$\Delta(r) = \frac{2}{3\beta} \begin{cases} r^3/r_*^3 \left(\sqrt{1 + \left(\frac{r_*}{r}\right)^3} - 1 \right), & r \geq R \\ R^3/r_*^3 \left(\sqrt{1 + \left(\frac{r_*}{R}\right)^3} - 1 \right), & r < R. \end{cases} \tag{2.15}$$

where $\mathfrak{g}_N$ is the Newtonian acceleration of the spherical mass, and r_* denotes a characteristic scale of the solution, the *Vainshtein radius*, determined by r_c and the Schwarzschild radius of the mass r_s:

$$r_*^3 = \frac{8\,r_c^2 r_s}{9\beta^2}. \tag{2.16}$$

Close to the mass ($r \ll r_*$), force modifications are suppressed by $\sim (r/r_*)^{3/2}$. At very large distances, $r \gg r_*$, $\Delta(r)$ approaches the constant $1/(3\beta)$, which exactly matches the linear solution, Eq. (2.8). Note that for the Sun and $r_c = 3000$ Mpc, $r_* \sim 75$ pc, while for the Milky way $r_* \sim$ Mpc. Hence, for $r_c \sim$ Gpc the non-linear interactions in Eq. (2.13) are expected to be important on cosmological scales. Thus it is crucial to self-consistently solve for the non-linearities in φ in conjunction with the evolution of structure in the Universe.

Another limiting case in which Eq. (2.13) is easily solvable is a plane wave density field: in this case, the two non-linear terms cancel, and one recovers the linearized solution. One might expect cosmological structure, with its sheets and filaments as well as virialized structures, to lie somewhere in between these limiting cases. Hence, the precise structure of the non-linearity in Eq. (2.13) is important for structure formation.

An order-of-magnitude estimate of where the coupling of the brane-bending mode becomes strong can be obtained as follows. We take the ratio of the linear and non-linear φ terms in Eq. (2.13) and evaluate them for the linear solution φ_L:

$$\frac{r_c^2}{3\beta\,a^2}(\nabla^2\varphi_L)^2 \,/\, \nabla^2\varphi_L = \frac{8\pi G\,r_c^2}{9\beta^2}\delta\rho = \frac{H_0^2 r_c^2}{3\beta^2}\Omega_m a^{-3}\,\delta \equiv g\,\delta, \tag{2.17}$$

One can then estimate that wherever $\delta \gtrsim \delta_{\rm th} \equiv g^{-1}$, the non-linear interactions of φ are important (see Fig. 3). The quantity g defined here is the non-linearity parameter introduced in Sec. IV C of [22]. At early times, $g \to 1/3$. By $z = 0$, it decreases to 10^{-3} and 10^{-2} in the nDGP–1 and nDGP–2 cosmologies, respectively, and ~ 0.1 in sDGP. Today then, the non-linearity criterion will be satisfied for $\delta \gtrsim O(1000)$ in the case of nDGP–1, and $O(100)$ in the case of nDGP–2, which will only be the case within the inner regions of dark matter halos. In the case of sDGP, $\delta_{\rm th} \approx 10$ today, which makes the non-linearities important in a significant fraction of the Universe [1].

D. Comparison with parametrized braneworld models

The nDGP+DE model presented here is a full consistent (albeit somewhat contrived) theory. It is worth comparing this model with the parametrized braneworld-inspired models introduced in [17, 18]. On sub-horizon scales, $k \gg aH, r_c$, these effective models yield the same equations as nDGP+DE (Section II B and II C), except for a modified function β:

$$\tilde{\beta}(a) = 1 + 2(Hr_c)^{2(1-\alpha)} \left(1 + \frac{\dot{H}}{3H^2} \right). \tag{2.18}$$

For $\alpha = 1/2$, this reduces to Eq. (2.9). Hence, the $\alpha = 1/2$ model of [18] is identical to our model on small scales. Although the $\alpha = 0$ model of [18] has a somewhat different linear growth rate, the structure of the φ equation is unchanged, and the behavior of the $\alpha = 0$ model is correspondingly very similar to that of the $\alpha = 1/2$ case [18]. Note that while the simulated models of [18] are similar to ours, the simulation technique is different: the simulations presented here solve the full φ equation (2.13), while [18] adopted an approximation neglecting the tensorial structure of Eq. (2.13). See Appendix A for a discussion.

On larger scales, $k \sim 1/r_c$, the full higher-dimensional theory becomes important. Parametrized generalizations of DGP were proposed in [17], which lead to interesting effects on the low multipoles of the CMB. In contrast, the nDGP+DE model exhibits the five-dimensional features of the DGP model on large scales, except of course for the expansion history which is ΛCDM. Higher-dimensional effects however should not be important for predictions on sub-horizon scales. In this regime, the results presented here for the nDGP+DE model will be relevant to generalized braneworld models as well.

III. SIMULATIONS

In [1], we have introduced cosmological simulations of the self-accelerating DGP model, which self-consistently solve the full non-linear Eq. (2.13) of the brane-bending mode. The code, based on an earlier version presented in [31], uses a standard particle-mesh algorithm, augmented by a relaxation solver for φ. The Gauss-Seidel relaxation proceeds using Newton's method. The convergence speed is greatly enhanced using multigrid techniques [32, 33]. We use this code for simulations of the nDGP+DE models, adapting the expansion history and the β [Eq. (2.9)] function as it appears in Eq. (2.13). See [1] for details on the implementation and tests of the code, which all apply in an analogous way to the nDGP+DE simulations.

We simulate two nDGP+DE models which only differ in their value of r_c, 500 Mpc in the case of nDGP–1, and 3000 Mpc for nDGP–2. The remaining cosmological parameters defining the expansion history and the primordial power spectrum are taken from the best-fit flat ΛCDM model given in [10]. The data used in their fit are the WMAP 5yr results, Supernova and H_0 measurements. Tab. I summarizes the cosmological parameters of the simulations.

In addition to the full simulations, we performed simulations for nDGP–1 and nDGP–2 using the linearized field equation for φ, by replacing G in the GR simulations with $G_{\rm lin}(a)$ given in Eq. (2.8). We refer to the latter as *linearized DGP* simulations. We also simulated a standard ΛCDM cosmology with identical expansion history. Deviations of the nDGP+DE simulations from the ΛCDM simulations are thus purely due to the modification of gravity. We have verified that our ΛCDM simulations match fitting formulas for the non-linear power spectrum and halo mass function. Since these results are essentially the same as those shown in [34, 35], we do not show them again here.

The simulations were started at $z_i = 49$. In order to test whether this is early enough to capture the non-linear evolution in our smallest box, we compared the power spectrum in that box after 10 time steps ($a = 0.04$) to the initial power spectrum ($a = 0.02$). The departures from scale-free linear evolution in the power spectrum are below 1% even up to $k = 2k_{\rm max} \approx 6\,h/{\rm Mpc}$. We conclude that given the limited resolution of our simulations, there is no need to start the simulations at an earlier time.

However, as can be seen from Eq. (2.8), there are small residual effects from DGP even at the initial epoch, where $\beta(z_i)$ is of order a few hundred. In order to take into account these small modified gravity effects, we correct the linear ΛCDM power spectrum at z_i as given by CAMB [36] by a factor $f^2(k)$ where $f(k) = T_{\rm PPF,DGP}(k, z_i)/T_{\Lambda\rm CDM}(k, z_i)$. Here, $T_{\rm PPF,DGP}$ is the DGP transfer function calculated in the parametrized Post-Friedmann approximation [30], which has been shown to be accurate at the few percent level on large scales. On small, quasi-static scales the calculation is exact. $T_{\Lambda\rm CDM}$ was calculated in the same way without any modification to gravity. Fig. 4 (left panel, solid line) shows the correction factor f obtained in this way as a function of k. At $z_i = 49$, the DGP effects on the transfer function are at the level of few 10^{-3}. Hence, a percent-level uncertainty on the correction will have a negligible impact on the initial power spectrum. Furthermore, for simplicity and because it is a small correction, we run all simulations including ΛCDM with the same initial conditions corrected for nDGP–1 ($r_c = 500$ Mpc).
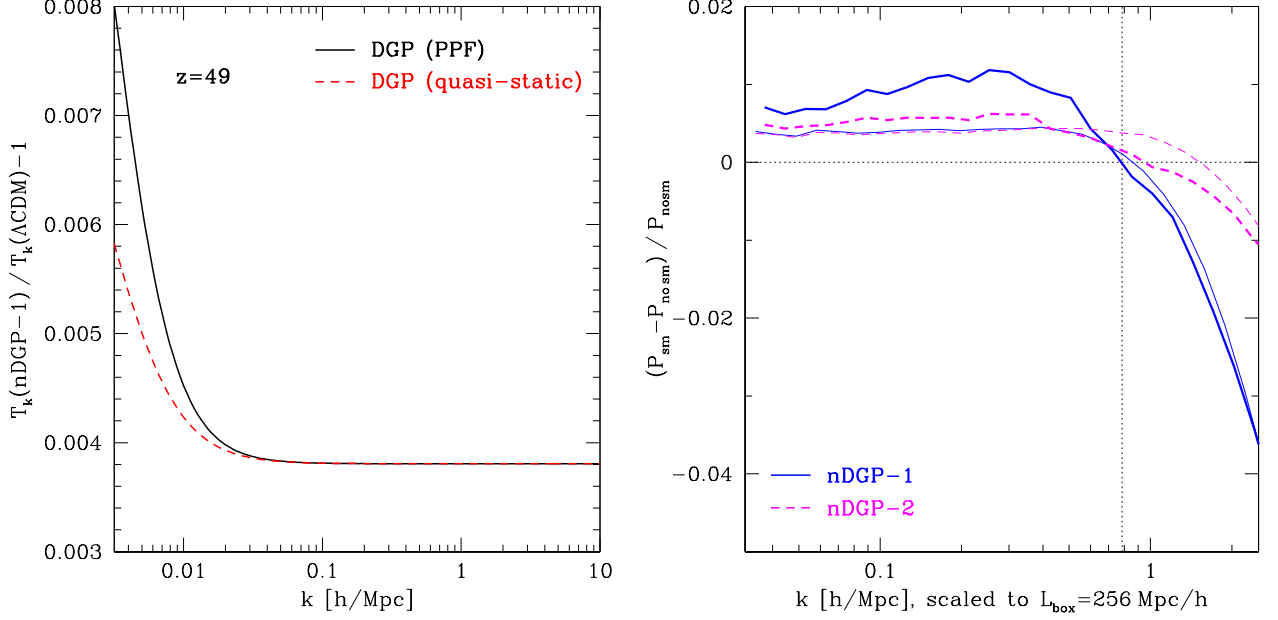
FIG. 4: *Left panel:* Deviation of the nDGP–1 matter transfer function from ΛCDM at the initial redshift of the simulations, $z_i = 49$. The solid line shows the PPF calculation for DGP which is used to correct the power spectrum for the initial conditions. The red dashed line shows the same deviation calculated using the quasi-static calculation [Eqs. (2.8)–(2.9)]. *Right panel:* Relative deviation of the matter power spectrum at $z = 0$ measured in simulations with Gaussian smoothing of the r.h.s of Eq. (2.13) to simulations without smoothing. The thick lines show results for $L_{box} = 400\,\mathrm{Mpc}/h$, while the thin lines show those for $L_{box} = 128\,\mathrm{Mpc}/h$. All k values were rescaled to those for a $256\,\mathrm{Mpc}/h$ box. The vertical dashed line shows the maximum wavenumber used in the analysis of the simulation results, $k_{max} = k_{Ny}/8$ (see text).

Fig. 4 (left panel) also shows the same correction calculated in the pure quasi-static approach [Eq. (2.8)], which neglects the non-local $\sqrt{k^2}/r_c$ term in the Poisson equation [18, 22]. On scales relevant for the simulations, the quasi-static approximation is accurate. This is important, since the N-body simulation assumes a quasi-static regime. Fig. 4 shows that this is justified at $z_i = 49$ for the nDGP models considered here (the deviations from the quasi-static assumption will continue to decline at later times).

Our simulations use a 512^3 grid with 512^3 particles. The high number of particles was chosen in order to reduce the shot noise in the density field. Since Eq. (2.13) is non-linear in the highest derivatives, it responds sensitively to small-scale inhomogeneities in the density field. Increasing the number of particles helps in reducing the residual

TABLE I: Cosmological parameters of the simulations.

	ΛCDM	nDGP–1	nDGP–2
$\Omega_m = 1 - \Omega_\Lambda$	0.259	0.259	0.259
r_c [Mpc]	∞	500	3000
Ω_{rc}	0	17.5	0.487
H_0 [km/s/Mpc]	71.6	71.6	71.6
$100\,\Omega_b\,h^2$		2.26	
$\Omega_c\,h^2$		0.110	
τ		0.0825	
n_s		0.959	
$A_s\ (k = 0.05\,\mathrm{Mpc}^{-1})$		$2.107\ 10^{-9}$	
$\sigma_8(\Lambda\mathrm{CDM})^a$		0.7892	

[a]Linear power spectrum normalization today of a ΛCDM model with the same primordial normalization.

TABLE II: Simulation type and number of runs per box size.

	L_{box} [Mpc/h]			
	400	256	128	64
ΛCDM	3	3	3	6
Linearized nDGP–1	3	3	3	6
Full nDGP–1	3	3	3	6
Linearized nDGP–2	3	3	3	6
Full nDGP–2	3	3	3	6
$k_{max} = k_{Ny}/8$ [h/Mpc]	0.50	0.79	1.57	3.14
r_{cell} [Mpc/h]	0.78	0.50	0.25	0.13
M_{min} [$10^{12}\,M_\odot/h$]	219	57.3	7.17	0.90
r_s [grid cells]^a	0.8	0.8	0.8	–

[a]Gaussian smoothing radius for full DGP simulations.

errors in the numerical solution of Eq. (2.13) to an acceptable level [1]. Note that we adopt a very strict (conservative) convergence criterion, in demanding that the dimensionless RMS residuals of the field equation are less than 10^{-10}. For the self-accelerating simulations presented in [1], we employed a Gaussian smoothing of the r.h.s. of Eq. (2.13). Fortunately, the convergence properties of the nDGP models considered here are better, since the cross-over scale is smaller: this raises the density threshold for which the non-linearities in φ become important. Correspondingly, particle noise in the density field has less impact. This can also be seen by considering the Vainshtein radius of a single particle in the simulations: for the self-accelerating model of [1], r_* was of order 1 grid cell. For the models considered here, it is less than 0.5 grid cells.

For this reason, we were able to eliminate the smoothing of the r.h.s. for our smallest box ($64\,\mathrm{Mpc}/h$ comoving size), where the smoothing effects are largest [1]. In addition, we lowered the smoothing radius to 0.8 grid cells for all other boxes. These choices were again made based on achieving an RMS residual less than 10^{-10} at all time steps. We quantified the effect of the smoothing by comparing full DGP simulations with and without smoothing, where the latter slightly violate our upper bound on the residuals (maximum residual of $\sim 3 - 6 \times 10^{-10}$). Fig. 4 (right panel) shows the power spectrum at $z = 0$ of simulations with smoothing relative to simulations without smoothing using the same initial conditions. The effects of the smoothing mainly appear on wavenumbers larger than the adopted maximum wavenumber, given by $k_{\mathrm{max}} = k_{\mathrm{Ny}}/8$, where k_{Ny} is the Nyquist frequency of the grid [1]. Below k_{max}, the differences are below 1.5%, significantly smaller than our statistical uncertainties on the final power spectrum measurement (Section IV A). The same was found for the halo mass function. Hence, no correction for smoothing effects is necessary.

Note that since the smoothing damps power in the brane-bending mode on small scales, and the brane-bending mode is attractive in the nDGP model, the simulations with smoothing of the r.h.s. have suppressed power on small scales. Fig. 4 also shows that the power spectrum is stable even for simulations that violate our adopted convergence criterion by a factor of 3-6. We simulated four different comoving box sizes, from $400\,\mathrm{Mpc}/h$ to $64\,\mathrm{Mpc}/h$. The number of runs for each model and box is summarized in Tab. II.

IV. RESULTS

A. Matter Power Spectrum

First, we compare the power spectrum measured in DGP simulations $P_{\mathrm{DGP}}(k)$ to that of the GR+DE simulations with the same expansion history, $P_{\Lambda\mathrm{CDM}}(k)$ (Fig. 5). The procedure is the same as that employed in [1, 34]: we calculate the relative deviation of the power spectrum run by run, comparing simulations with identical initial conditions. We then determine the average deviation and its error by bootstrapping over realizations. In this way we are able to reduce the variance of the deviations considerably.

The left panel in Fig. 5 shows the results for full and linearized simulations of the nDGP–1 cosmology at redshift 0. Both simulations approach the scale-invariant linear predictions on the largest scales ($k \lesssim 0.1\,h/\mathrm{Mpc}$). For nDGP–1 on non-linear scales, we find good overall agreement with the results of Khoury & Wyman (Fig. 11 in [18]). This is expected, since we found that the effects on the power spectrum of the G_{eff}–approximation used in [18] are at the level of 5–10 percent in our moderate resolution simulations (Appendix A). The overall scale-dependence of the deviations in the non-linear matter power spectrum shows the typical behavior when comparing a cosmology with the same linear power spectrum shape but slightly different normalization. The deviations initially grow towards smaller scales, peak around $k \sim 0.7\,h/\mathrm{Mpc}$, and then decline again towards even smaller scales. At the peak, the matter power spectrum in nDGP–1 is enhanced by a factor of 2 with respect to ΛCDM, while the enhancement is about 65% in the linear regime. In the halo model, the largest deviations occur at a scale roughly corresponding to the transition region between two-halo and one-halo terms. On smaller scales, the power spectrum mainly probes the density profiles of dark matter halos. If the halo profiles are not strongly affected by the increased growth, the deviations are expected to decrease again in this regime (see Section IV C for a study of halo profiles). These trends are captured qualitatively by the `halofit` prescription [37], which is used to map a linear power spectrum into a non-linear one and is calibrated on GR N-body simulations. The dashed line in Fig. 5 shows the deviation of the non-linear $P(k)$ for DGP from that for ΛCDM obtained using `halofit` with the corresponding linear power spectra. While the `halofit` predictions reproduce the qualitative behavior, the overall magnitude of the deviations on non-linear scales is not matched. Interestingly, `halofit` does predict the slight suppression of the deviations *below* the linear prediction on quasi-linear scales $k \lesssim 0.1\,h/\mathrm{Mpc}$. A modification of the `halofit` parameters to improve the fit to modified gravity simulations was presented in [18]. Note that if there was a unique prescription to go from linear power spectrum to the non-linear one *at a fixed redshift*, then `halofit` should be able to describe the linearized DGP simulations, as the linear power spectrum in the nDGP+DE model is equivalent to a ΛCDM power spectrum with a slightly higher normalization on these scales ($k \gtrsim 0.01\,h/\mathrm{Mpc}$). The discrepancy between the linearized DGP simulations and the
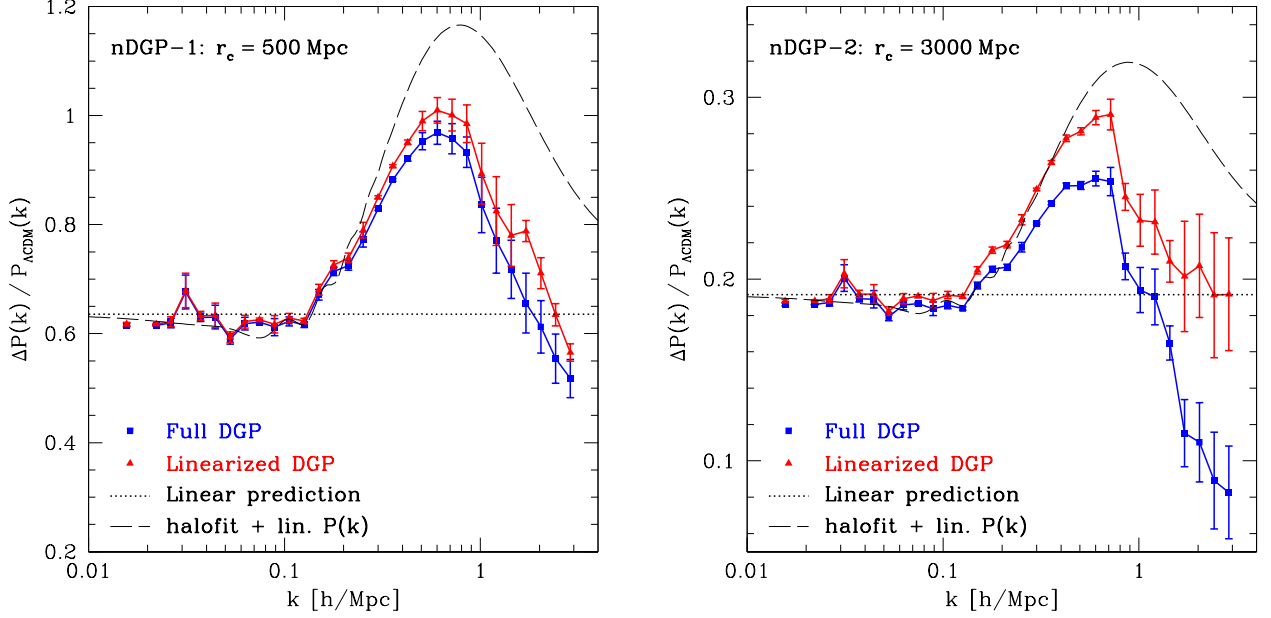
FIG. 5: Relative deviation in the matter power spectrum from ΛCDM at $z = 0$, $\Delta P(k)/P_{\Lambda\text{CDM}}(k) \equiv (P_{\text{DGP}}(k) - P_{\Lambda\text{CDM}}(k))/P_{\Lambda\text{CDM}}(k)$ for nDGP–1 *(left panel)* and nDGP–2 *(right panel)*. The blue squares and red triangles show the measurements from the full and linearized DGP simulations, respectively. The short-dashed line shows the almost scale-invariant deviation predicted using linear perturbation theory (Section II B), while the long-dashed line shows the deviation obtained when using the `halofit` prescription together with the linear prediction for DGP.

`halofit` prediction shows that the linear-to-nonlinear mapping does depend on the growth *history* (which is different in nDGP+DE), rather than just the growth factor at the present time.

For nDGP–1, the deviations from GR in the full simulations are only marginally suppressed compared to those in the linearized simulations, on the scales accessible to our simulations. This is somewhat expected, since the threshold overdensity for the Vainshtein mechanism in nDGP–1 is ~ 1000 (Section II C), which is only reached in the cores of the most massive halos in our simulations. The situation is slighly different in nDGP–2 (right panel of Fig. 5): here the effects of the non-linear interactions of φ are noticeable for $k \gtrsim 0.2\,h/\text{Mpc}$, and become increasingly important towards smaller scales. The behavior as function of k of the deviation in non-linear matter power is very similar to that of nDGP–1, with the overall magnitude being smaller ($20 - 30\%$).

Note that in both nDGP cosmologies, the power spectrum deviation becomes significantly scale-dependent at around $k \sim 0.1\,h/\text{Mpc}$, in the region where the second and higher harmonics of the baryon acoustic oscillations (BAO) are located. This scale-dependence should be taken into account when using (sufficiently precise) BAO measurements to constrain DGP and other braneworld models.

B.   Halo Mass Function

Previous studies have shown that the abundance of dark matter halos is a sensitive probe of modifications of gravity [1, 26, 35]. We identify dark matter halos in the DGP and GR+DE simulations using a spherical overdensity halo finder as described in [35], with the same mass thresholds as adopted in [1], corresponding to a minimum of 6400 particles in a halo (see Tab. II for the minimum halo mass for each box size). The halo mass M_{200} is defined as the mass contained within a spherical region of radius r_{200} around the halo center of mass, whose average density is $200 \times \overline{\rho}_m$. We calculate the mass function deviation of the nDGP simulations from the GR simulations run-by-run, and then take the average, as done for the power spectrum.

Fig. 6 shows the relative deviation of the mass function $n_{\ln M} \equiv dn/d\ln M$ in DGP from ΛCDM, where $n(M)$ is the number density of halos of a given mass. The left panel shows the result for nDGP–1, the right panel for nDGP–2. In each case, the top panel shows the deviation at $z = 0$, while the bottom panel shows $z = 1$. The qualitative behavior is the same in all cases and is expected: the increase in halo abundance grows rapidly with mass, as the abundance of massive halos is exponentially sensitive to the amplitude of fluctuations today, which is increased in the nDGP
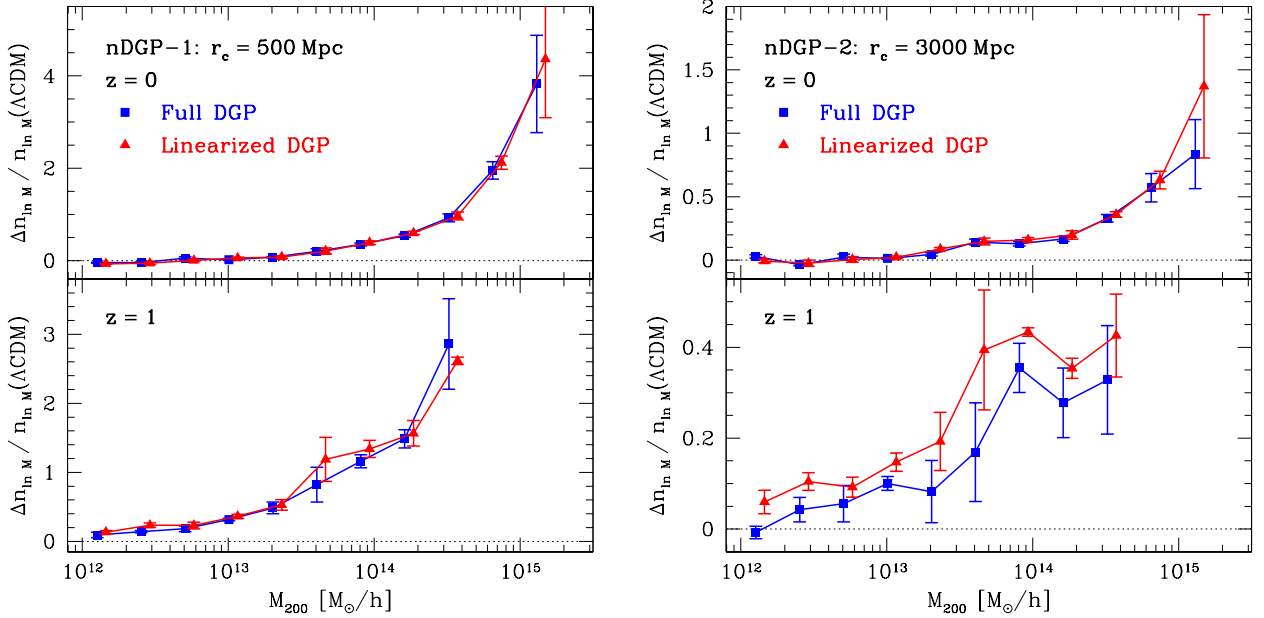
FIG. 6: Relative deviation of the halo mass function from ΛCDM, $\Delta n_{\ln M}/n_{\ln M}(\Lambda\text{CDM})$ where $\Delta n_{\ln M} \equiv n_{\ln M}(\text{DGP}) - n_{\ln M}(\Lambda\text{CDM})$, at $z = 0$ (*top*) and $z = 1$ (*bottom*) for nDGP–1 (*left panel*) and nDGP–2 (*right panel*). Blue squares and red triangles denote the full and linearized DGP simulations, respectively.

cosmologies. Since the abundance of massive halos can be probed using galaxy clusters, this observable can serve as a sensitive probe of braneworld gravity. Current observations should be able to put a lower limit on the cross-over scale r_c in the Gpc range, a constraint which would be independent of the specific DGP expansion history.

Note that at a fixed mass, the relative enhancement of the mass function at $z = 1$ is comparable to the one at $z = 0$. This is due to a cancelation of two effects: the growth enhancement in nDGP is smaller at $z = 1$ than at $z = 0$; on the other hand, a fixed mass corresponds to a rarer fluctuation at $z = 1$ than at $z = 0$, hence increasing the sensitivity to the growth enhancement.

At $z = 0$, the Vainshtein mechanism does not strongly affect the halo mass functions in our nDGP+DE simulations. For nDGP–2, there is an indication of a slightly suppressed abundance of the highest mass halos in the full simulations compared to the linearized simulations, which one expects since the most massive halos have the largest effective Vainshtein radii. This situation changes somewhat at higher redshifts: in nDGP–2 at $z = 1$, the mass function in the full simulations is lower by $5 - 10\%$ at all masses. This can be explained by the lower threshold overdensity at which the φ self-coupling becomes important (Section II C): in nDGP–2, the non-linearity parameter g is ~ 0.06 at $z = 1$, compared to 0.01 at $z = 0$. Since a much larger portion of the universe has $\delta \gtrsim 10$ rather than $\delta \gtrsim 100$, the self-coupling of φ affects a broad range of halo masses at $z = 1$.

C. Halo Profiles

Once dark matter halos have been identified, we can study the distribution of mass around them. We stack the radially averaged density profiles of halos in mass intervals as described in [35]. The center-of-mass of each halo is calculated as the center of mass of particles within $1.4\,r_{\text{cell}}$ of the center of the central (highest density) cell, which comprise a large fraction of the halo mass. In order to reduce scatter within the mass bin, we scale each density profile to its own r_{200} before stacking. We then bootstrap over all halos in the given mass range in order to determine the average profile. The spatial resolution of our particle-mesh simulations is limited by the fixed size of grid cells r_{cell} (see Tab. II). We measure halo profiles down to the grid scale, though we expect that profiles have converged only at scales of several grid cells. We only use the highest resolution boxes ($L_{\text{box}} = 64\,\text{Mpc}/h$) for the profile measurements.

Fig. 7 (upper panels) shows the halo density profiles measured in the full DGP simulations, in three mass bins: $10^{12} - 10^{13}\,M_\odot/h$ (left), $10^{13} - 10^{14}\,M_\odot/h$ (center), $10^{14} - 10^{15}\,M_\odot/h$ (right). In the inner regions, $r \lesssim r_{200}$, all DGP simulations show the same, universal profile. Moreover, the profiles match those of the corresponding GR+DE simulations, as shown in the lower panels in Fig. 7. This is because the inner regions of halos are assembled early
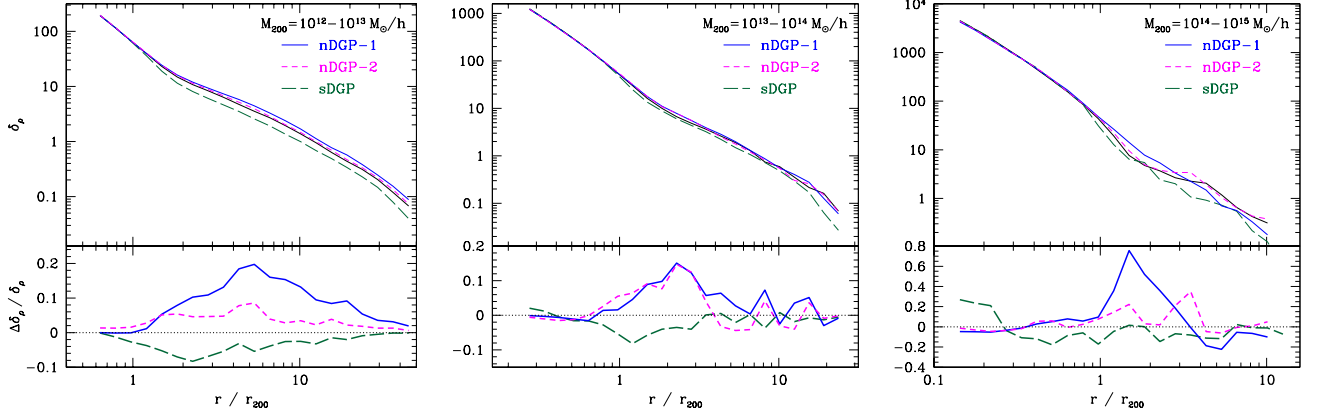
FIG. 7: Average halo density profiles measured in the full DGP simulations. Each figure corresponds to a fixed mass range: $\lg M/M_\odot/h = 12 - 13$ (left), $13 - 14$ (middle), $14 - 15$ (right). The top panels show profiles of $\delta_\rho \equiv (\rho - \overline{\rho}_m)/\overline{\rho}_m$ vs. r in units of r_{200}, while the bottom panel shows the relative deviation from the GR simulation with the same expansion history in each case (ΛCDM for nDGP, QCDM for sDGP). For all figures, individual halo profiles were scaled to their respective r_{200} before averaging.

on in the history of the universe, where the effects of the brane-bending mode are very small ($\beta \gg 1$). Though our simulations cannot probe deep into the halos, it seems unlikely there will be significant departures from GR at still smaller radii.

Outside of the virial radius of halos, where matter is still infalling and tidal fields are important, modified gravity effects can be seen: the departures from the GR simulations typically peak around $2 - 3\,r_{200}$, and decrease again towards larger radii. As expected, they are positive for the nDGP+DE simulations, largest for nDGP–1, and negative for sDGP. Note that the profiles for the highest mass bin are noisy due to small halo statistics (especially in the case of sDGP where the abundance of massive halos is significantly suppressed). For $r \gtrsim r_{200}$, Fig. 7 should be interpreted as a halo-mass correlation function (scaled to r_{200}), which is related to the mass correlation function and power spectrum. Hence, the enhancement of the halo-mass correlation function in the nDGP simulations, peaking at a few r_{200}, is another way of seeing the power spectrum enhancement, peaking at $k \sim 0.7\,h/$Mpc (Fig. 5).

We can also look at the behavior of the brane-bending mode within halos. Fig. 8 (top panel) shows the average profile of the radial gradient $|\nabla_r \varphi| \times 3\beta/2$ measured in the full DGP simulations around the most massive (and best-resolved) halos. We show the gradient of φ as the quantity with observable effects, since φ itself is not observable. The prefactor is chosen so that the quantity approaches $\nabla_r \Phi_-$ on linear scales (Section II B). Clearly, φ and its gradient are suppressed within halos. As expected, the suppression is most severe for sDGP, and weakest for nDGP–2. In each case, the thin dashed lines in Fig. 8 show the approximate solution for φ presented in [18], calculated given the density field as described in [1] (see also Appendix A). While the approximation works well at the very center of the halos, it does not describe the solution at $r \gtrsim 0.5\,r_{200}$. Moreover, the discrepancy becomes larger the stronger the non-linearities in the φ equation are, i.e. the larger r_c is.

The lower panel of Fig. 8 shows the gradient of the dynamical potential around the same halos compared to the gradient of the Newtonian or lensing potential $\Psi_N = \Phi_-$ which obeys the usual, unmodified Poisson equation. A discrepancy between the dynamical potential of a given mass and its lensing potential is precisely the quantity that is constrained by Solar System tests, described via the post-Newtonian parameter γ [38]. Fig. 8 shows that this deviation is indeed suppressed within massive halos in our simulations, although the simulations lack the resolution to follow the suppression very far into the cores of halos. As expected, the suppression is strongest for sDGP which has the largest non-linearity parameter g (Section II C), and weakest for nDGP–1.

D. Bispectrum

The matter bispectrum in DGP is, in principle, a probe of the quadratic non-linearity in the brane-bending mode equation. This non-linearity adds an additional contribution to the tree-level bispectrum generated by the ordinary gravitational non-linearities [22]. As discussed in Section II C, the specific quadratic self-interactions of the brane-bending mode lead to a dependence on geometry. In Fourier space, the non-linearity in Eq. (2.13) leads to a coupling between two Fourier modes $\tilde{\varphi}(\mathbf{k}_1)$, $\tilde{\varphi}(\mathbf{k}_2)$ with a kernel proportional to $1 - (\hat{k}_1 \cdot \hat{k}_2)^2$, where $\hat{k}_i$ denote unit vectors of
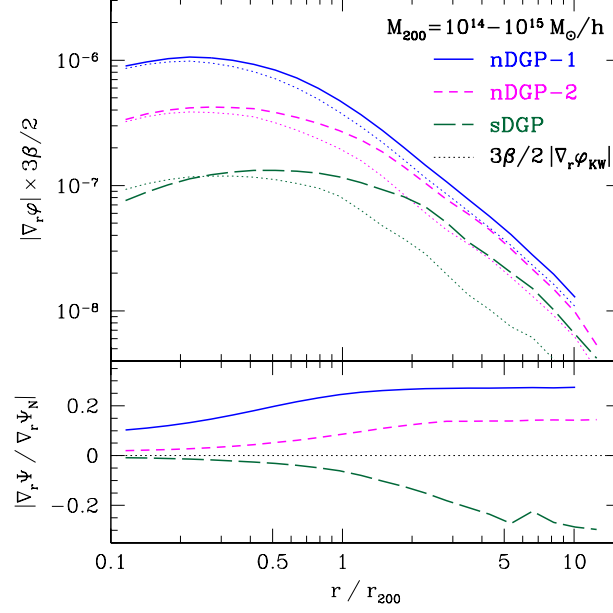
FIG. 8: *Top panel:* Average profiles of the radial gradient of φ, i.e. the force modification, measured in the full DGP simulations and scaled by $3\beta/2$, for halos of mass $\lg M / M_\odot/h = 14 - 15$. The profiles were averaged in a similar way as the density profiles. *Bottom panel:* Deviation of the dynamical potential Ψ [Eq. (2.10)] from the Newtonian potential or lensing potential $\Phi_- = \Psi_N$ [Eq. (2.12)] around the same dark matter halos. This quantity is probed by Solar System tests.
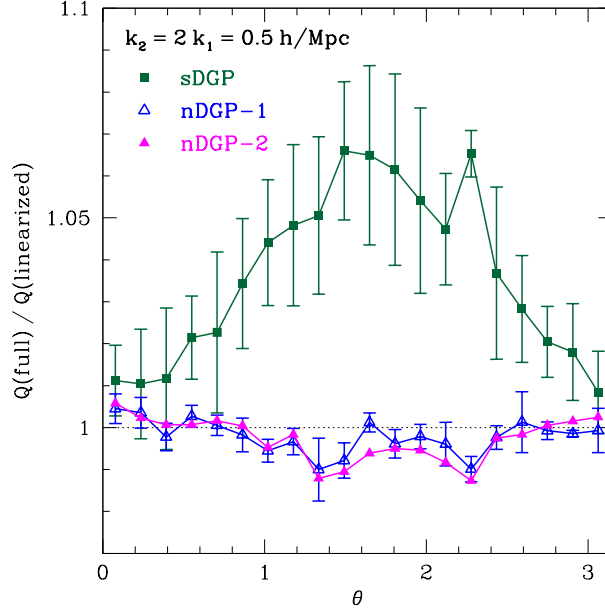
FIG. 9: Ratio of the reduced bispectrum measured in full and linearized DGP simulations, vs the angle between the wavevectors $\mathbf{k}_1 = 0.5\,h/\mathrm{Mpc}$, $\mathbf{k}_2 = 1\,h/\mathrm{Mpc}$. This is a direct probe of the configuration dependence of the Vainshtein effect. For each model, the bispectra were measured in the $256\,\mathrm{Mpc}/h$ boxes. The errors are bootstrap error bars on the ratio determined from the different runs. We have omitted the error bars on the nDGP–2 model for clarity - they are very similar to those for nDGP–1.

the respective wavenumbers. As shown in [22], this structure manifests itself as a characteristic change of the shape

dependence of the bispectrum, which is commonly expressed in terms of the reduced bispectrum Q:

$$Q(\mathbf{k}_1, \mathbf{k}_2, \mathbf{k}_3) \equiv \frac{B(\mathbf{k}_1, \mathbf{k}_2, \mathbf{k}_3)}{P(\mathbf{k}_1)P(\mathbf{k}_2) + P(\mathbf{k}_2)P(\mathbf{k}_3) + P(\mathbf{k}_3)P(\mathbf{k}_1)}, \tag{4.1}$$

where $B(\mathbf{k}_1, \mathbf{k}_2, \mathbf{k}_3)$ is the bispectrum. In order to separate these characteristic effects of the brane-bending mode interactions as cleanly as possible from the ordinary gravitational non-linearities, we compare the bispectrum measured in the full DGP simulations to that of the linearized DGP simulations, which have an identical linear growth factor, and hence are very similar in their state of non-linear evolution. Fig. 9 shows the ratio of the reduced bispectrum measured in the two cases, for fixed wavenumbers of $k_1 = 0.25\,h/\mathrm{Mpc}$ and $k_2 = 0.5\,h/\mathrm{Mpc}$, as a function of the angle between them, $\cos\theta = \hat{k}_1 \cdot \hat{k}_2$. The bispectrum was measured in the simulations using Monte Carlo integration in a very similar way as described in [39]. We again average the ratios run-by-run, and estimate error bars by bootstrapping over realizations.

The strongest effects are seen for the sDGP case, since this cosmology has the largest r_c and hence the lowest threshold for the onset of the φ self-interactions. Note that the bispectrum is enhanced in the full sDGP simulations for equilateral configurations $\theta \approx \pi/2$, while it is very close to the linearized simulations for squeezed configurations $\theta = 0,\ \pi$. For squeezed configurations, which correspond to planar geometry, the kernel $1 - (\hat{k}_1 \cdot \hat{k}_2)^2 = 0$ and the non-linearities vanish. For equilateral configurations, the suppression of φ is strongest, which leads to an enhanced bispectrum in the full DGP simulations since the brane-bending mode is repulsive. For nDGP–1 and nDGP–2, we see a hint of the opposite effect: here φ is attractive, and a suppression due to the self-interactions in equilateral configurations leads to a suppression of the bispectrum relative to the linearized simulations. The overall effect is much smaller, since r_c is smaller and the non-linearities in φ only become important at higher densities (i.e., smaller scales).

The result for the sDGP bispectrum agrees very well with that found in [26]. Note that lacking very large box sizes, we measure the bispectrum at relatively small scales. The ordinary gravitational non-linearities which enter at higher order already contribute at the percent level on the scales accessible in our simulations. Hence, we do not attempt a quantitative comparison with tree-level perturbation theory predictions here.

V. DISCUSSION

We have introduced the nDGP+DE model based on the normal branch of DGP with a smooth dark energy component on the brane, which results in an expansion history that is precisely ΛCDM. This model can serve as an approximation, especially on sub-horizon scales, to more general braneworld models whose cosmological solutions have not been obtained yet. In addition, the $r_c \to \infty$ limit precisely corresponds to General Relativity plus cosmological constant.

Geometric measurements such as the acoustic scale constrained from the CMB, BAO, and Supernovae observations do not constrain the crossover scale r_c between 4D and 5D gravity in this scenario. The growth of large-scale structure however does offer a sensitive probe of braneworld gravity via the effects of the brane-bending mode which mediates an additional attractive force. In the case of the self-accelerating branch, the brane-bending mode is repulsive, so that the modified gravity effects are sign-flipped.

In order to study the formation of structure in these models, it is necessary to solve the non-linear equations of the brane-bending mode in conjunction with the ordinary gravitational dynamics in N-body simulations [1]. These non-linear interactions, which are responsible for the Vainshtein mechanism [23, 24] restoring General Relativity in high density environments, also leave characteristic signatures in the bispectrum in the simulations [22], which we have found in both sDGP and nDGP simulations. In addition, the non-linearities manifest themselves in a suppression of the brane-bending mode around massive halos.

The matter power spectrum in nDGP+DE shows a characteristic enhancement compared to that of ΛCDM, increasing towards smaller scales up to $k \sim 0.7\,h/\mathrm{Mpc}$, and decreasing on even smaller scales. This is evidenced in a complementary way by the profiles of dark matter halos and their environments (halo-mass correlation function). Similar to what was found in $f(R)$ simulations [35], the inner regions of halos are not affected by the enhanced forces since they assembled at early times. The strongest effects are seen in the near environment of halos, around $2 - 3\,r_{200}$, corresponding to the scale where the power spectrum enhancement peaks.

The abundance of massive halos is known to be a sensitive probe of the growth of structure [35, 40–42]. We found that indeed massive clusters are $2 - 4$ times more numerous for the nDGP+DE model with $r_c = 500 - 3000\,\mathrm{Mpc}$. Current cluster abundance measurements (e.g. [43–45]) should be able to constrain the crossover scale r_c to be at least of order Gpc - a constraint which can be placed independently of the specific DGP expansion history.

As the next step in understanding the effects of braneworld gravity on large scale structure, an upcoming paper will detail a model of the matter power spectrum and halo mass function based on spherical collapse and the halo

model. Such a model can also serve as an efficient way of dealing with cosmological parameter dependencies when comparing with actual observations [27]. In the future, by means of these simulations and a physical model of their results, we will hopefully be able to probe the next generation of braneworld scenarios via their effect on the growth of cosmic structure.

Appendix A: Comparison with $G_{\rm eff}(\delta)$ approximation

We now discuss the approximation adopted in the simulations of [18] and compare it with the results of our full solution of the brane-bending mode equation (2.13). Consider a spherical "tophat" mass with a constant density contrast $\delta\rho$. Then, the ansatz $\varphi(r) = A\, r^2 + C$ solves Eq. (2.13), and in particular we have:

$$(\nabla_i \nabla_j \varphi)^2 = \frac{1}{3}(\nabla^2 \varphi)^2. \tag{A1}$$

For this special case, the non-linear terms combine to an equation of φ which is algebraic in $\nabla^2 \varphi$:

$$\nabla^2 \varphi + \frac{2r_c^2}{9\beta\, a^2}(\nabla^2 \varphi)^2 = \frac{8\pi G a^2}{3\beta}\bar{\rho}_m \delta. \tag{A2}$$

This can then be solved for $\nabla^2 \varphi$ in terms of a non-analytic function of the overdensity δ:

$$\nabla^2 \varphi \; = \; 8\pi G_{\rm eff}(\delta)\, a^2 \bar{\rho}_m \delta, \tag{A3}$$

$$G_{\rm eff} \; = \; \frac{2}{3\beta}\frac{\sqrt{1+\varepsilon}-1}{\varepsilon}, \quad \varepsilon \equiv \frac{8H_0^2 r_c^2}{9\beta^2}\Omega_m a^{-3}\delta. \tag{A4}$$

Thus, the brane-bending mode is determined in this approximation by a Poisson equation with density-dependent gravitational constant $G_{\rm eff}(\delta)$. Since this is a linear equation in φ which can be solved via Fourier transform, a simulation using this approximation is similar in terms of computing time as ordinary GR simulations, and much less computationally expensive than solving the full non-linear differential φ equation.

We now discuss the caveats of this "$G_{\rm eff}$ approximation". For more general density profiles $\delta\rho \neq$ const., Eq. (A3) is only an approximate solution. More importantly, as already pointed out in [18], the approximation does not have the correct large-distance behavior even for an isolated top-hat mass, so that scales in the linear regime of cosmological perturbations can in principle be affected by this incorrect behavior.

To see this, consider an isolated mass with $\delta\rho = 0$ for r larger than some radius R. Integrating Eq. (2.13) over a sphere with radius $r > R$, we see that the two non-linear terms in Eq. (2.13) cancel via partial integration, leaving only boundary terms which become increasingly suppressed as we let $r \to \infty$. Since the right-hand side is just proportional to the enclosed mass M within r, we see that φ approaches the linearized solution $\varphi(r) = (2/3\beta)GM/r$ at large r, irrespective of the strong non-linearities close to the mass. For this reason, we recover the linear predictions of the DGP model (Section II B) on large scales in the simulations.

In contrast, integrating Eq. (A3) over the sphere with radius $r > R$, we see that the asymptotic behavior in this approximation is $\varphi(r) \to (2/3\beta)\overline{G_{\rm eff}}M/r$, where $\overline{G_{\rm eff}}$ is the effective gravitational constant averaged over the mass. As Eq. (A4) shows, $G_{\rm eff} \ll G$ if the density contrast $\delta \gg 1$. Hence, the far field of φ is strongly suppressed in this approximation. In particular, if most of the cosmological mass is in non-linear structures with $\delta > 1$, we do not expect to recover linear theory predictions on large scales in this approximation.

As this discussion shows, the error encurred with the $G_{\rm eff}(\delta)$ approximation in cosmological N-body simulations depends on the resolution of the simulations: very low resolution simulations (with large box sizes) which resolve little non-linear structure will not be affected; high-resolution simulations which resolve very small dark matter
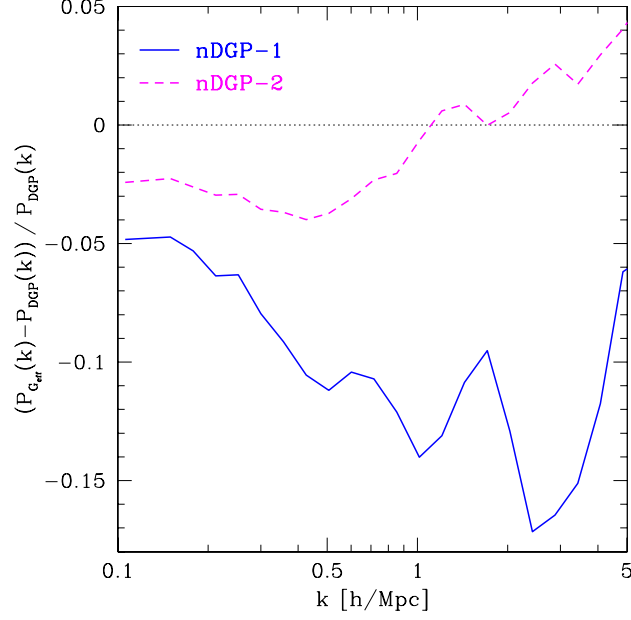
FIG. 10: Relative deviation of the power spectrum at $z = 0$ measured in a simulation using the $G_{\rm eff}(\delta)$ approximation, $P_{G_{\rm eff}}$, from that of the full DGP simulation, $P_{\rm DGP}(k)$ for nDGP–1 and nDGP–2. In each case, results are shown for a "typical" run with $L_{\rm box} = 64\,{\rm Mpc}/h$.

halos will show a strong suppression of the φ field and the corresponding modified forces on large scales, if the $G_{\rm eff}$ approximation is used. In order to test how big the effect is in our moderate resolution simulations, we reran a representative simulation of our smallest box ($L_{\rm box} = 64\,{\rm Mpc}/h$) for the nDGP–1 and nDGP–2 models using Eq. (A3) instead of Eq. (2.13). For this, we chose a realization with a power spectrum close to the average of our 6 realizations of the $64\,{\rm Mpc}/h$ box. Fig. 10 shows the relative deviation in the power spectrum at $z = 0$ in simulations with the $G_{\rm eff}$ approximation from that of the full DGP simulation with the same initial conditions, for nDGP–1 and nDGP–2. The deviations are around 5–10% for nDGP–1 and $\sim 3\%$ for nDGP–2. The magnitude of deviations is noticeable given our $\lesssim 1\%$ precision on the power spectrum deviation on quasilinear scales (Fig. 5). As expected from our discussion, the deviations persist on the largest scales probed by this box size. Furthermore, power is suppressed in the $G_{\rm eff}$ simulations due to the suppression of the attractive φ-mediated force. The deviations are larger in nDGP–1 simply due to the stronger effect of φ on structure formation in the small-r_c model. Thus, while the use of the $G_{\rm eff}(\delta)$ approximation would not have a dramatic impact on the main results presented in this paper, care must be taken in future high-resolution simulations of braneworld models: the artefacts of this approximation will increase rather than shrink with increasing resolution.

[1] F. Schmidt, Phys. Rev. D **80**, 043001 (2009), 0905.0858.
[2] C. Deffayet, Physics Letters B **502**, 199 (2001), arXiv:hep-th/0010186.
[3] C. Deffayet, S. J. Landau, J. Raux, M. Zaldarriaga, and P. Astier, Phys. Rev. D **66**, 024019 (2002), arXiv:astro-ph/0201164.
[4] G. Dvali, S. Hofmann, and J. Khoury, Phys. Rev. D **76**, 084006 (2007), arXiv:hep-th/0703027.
[5] C. de Rham, S. Hofmann, J. Khoury, and A. J. Tolley, Journal of Cosmology and Astro-Particle Physics **2**, 11 (2008), 0712.2821.
[6] G. Dvali, G. Gabadadze, and M. Porrati, Physics Letters B **485**, 208 (2000), arXiv:hep-th/0005016.
[7] M. A. Luty, M. Porrati, and R. Rattazzi, Journal of High Energy Physics **2003**, 029 (2003), URL http://stacks.iop.org/1126-6708/2003/i=09/a=029.
[8] A. Nicolis and R. Rattazzi, Journal of High Energy Physics **6**, 59 (2004), arXiv:hep-th/0404159.
[9] R. Gregory, N. Kaloper, R. C. Myers, and A. Padilla, Journal of High Energy Physics **10**, 69 (2007), 0707.2666.
[10] W. Fang, S. Wang, W. Hu, Z. Haiman, L. Hui, and M. May, Phys. Rev. D **78**, 103509 (2008), 0808.2208.
[11] V. Sahni and Y. Shtanov, Journal of Cosmology and Astro-Particle Physics **11**, 14 (2003), arXiv:astro-ph/0202346.
[12] A. Lue and G. D. Starkman, Phys. Rev. D **70**, 101501 (2004).
[13] T. Giannantonio, Y.-S. Song, and K. Koyama, Phys. Rev. D **78**, 044017 (2008), 0803.2238.
[14] L. Lombriser, W. Hu, W. Fang, and U. Seljak, ArXiv e-prints (2009), 0905.1112.
[15] A. Nicolis, R. Rattazzi, and E. Trincherini, Phys. Rev. D **79**, 064036 (2009), 0811.2197.
[16] G. Gabadadze, ArXiv e-prints (2009), 0908.1112.
[17] N. Afshordi, G. Geshnizjani, and J. Khoury, ArXiv e-prints (2008), 0812.2244.
[18] J. Khoury and M. Wyman, ArXiv e-prints (2009), 0903.1292.
[19] K. Koyama and R. Maartens, Journal of Cosmology and Astro-Particle Physics **1**, 16 (2006), arXiv:astro-ph/0511634.
[20] Y.-S. Song, I. Sawicki, and W. Hu, Phys. Rev. D **75**, 064003 (2007).
[21] A. Cardoso, K. Koyama, S. S. Seahra, and F. P. Silva, Physical Review D (Particles, Fields, Gravitation, and Cosmology) **77**, 083512 (pages 16) (2008), URL http://link.aps.org/abstract/PRD/v77/e083512.
[22] R. Scoccimarro, ArXiv e-prints (2009), 0906.4545.
[23] A. I. Vainshtein, Physics Letters B **39**, 393 (1972), ISSN 0370-2693.
[24] C. Deffayet, G. Dvali, G. Gabadadze, and A. Vainshtein, Phys. Rev. D **65**, 044026 (2002), arXiv:hep-th/0106001.
[25] K. Koyama and F. P. Silva, Phys. Rev. D **75**, 084040 (2007), arXiv:hep-th/0702169.
[26] K. C. Chan and R. Scoccimarro, ArXiv e-prints (2009), 0906.4548.
[27] F. Schmidt, A. Vikhlinin, and W. Hu, ArXiv e-prints (2009), 0908.2457.
[28] S. Bag, S. S. Mishra, and V. Sahni, Phys. Rev. D **97**, 123537 (2018), URL https://link.aps.org/doi/10.1103/PhysRevD.97.123537.
[29] A. Lue, R. Scoccimarro, and G. D. Starkman, Phys. Rev. D **69**, 124015 (2004), arXiv:astro-ph/0401515.
[30] W. Hu and I. Sawicki, Phys. Rev. D **76**, 104043 (2007), arXiv:0708.1190.
[31] H. Oyaizu, Phys. Rev. D **78**, 123523 (2008), 0807.2449.
[32] A. Brandt, Math. Comput. **31**, 333 (1977).
[33] W. L. Briggs, V. E. Henson, and S. F. McCormick, *A multigrid tutorial (2nd ed.)* (Society for Industrial and Applied Mathematics, Philadelphia, PA, USA, 2000), ISBN 0-89871-462-1.
[34] H. Oyaizu, M. Lima, and W. Hu, Phys. Rev. D **78**, 123524 (2008), 0807.2462.
[35] F. Schmidt, M. Lima, H. Oyaizu, and W. Hu, Phys. Rev. D **79**, 083518 (2009), 0812.0545.
[36] A. Lewis, A. Challinor, and A. Lasenby, Astrophys. J. **538**, 473 (2000), astro-ph/9911177.
[37] R. E. Smith, J. A. Peacock, A. Jenkins, S. D. M. White, C. S. Frenk, F. R. Pearce, P. A. Thomas, G. Efstathiou, and H. M. P. Couchman, MNRAS **341**, 1311 (2003), arXiv:astro-ph/0207664.
[38] C. M. Will, Living Reviews in Relativity **9**, 3 (2006), arXiv:gr-qc/0510072.
[39] R. Scoccimarro, S. Colombi, J. N. Fry, J. A. Frieman, E. Hivon, and A. Melott, Astrophys. J. **496**, 586 (1998), arXiv:astro-ph/9704075.
[40] S. D. M. White, J. F. Navarro, A. E. Evrard, and C. S. Frenk, Nature (London) **366**, 429 (1993).
[41] V. R. Eke, S. Cole, C. S. Frenk, and J. Patrick Henry, MNRAS **298**, 1145 (1998), arXiv:astro-ph/9802350.
[42] S. Borgani, P. Rosati, P. Tozzi, S. A. Stanford, P. R. Eisenhardt, C. Lidman, B. Holden, R. Della Ceca, C. Norman, and G. Squires, Astrophys. J. **561**, 13 (2001), arXiv:astro-ph/0106428.
[43] A. Vikhlinin, A. V. Kravtsov, R. A. Burenin, H. Ebeling, W. R. Forman, A. Hornstrup, C. Jones, S. S. Murray, D. Nagai, H. Quintana, et al., Astrophys. J. **692**, 1060 (2009), 0812.2720.
[44] E. Rozo, R. H. Wechsler, E. S. Rykoff, J. T. Annis, M. R. Becker, A. E. Evrard, J. A. Frieman, S. M. Hansen, J. Hao, D. E. Johnston, et al., ArXiv e-prints (2009), 0902.3702.
[45] A. Mantz, S. W. Allen, D. Rapetti, and H. Ebeling, ArXiv e-prints (2009), 0909.3098.